Stochastic Gravitational-Wave Signatures of Dark-Matter Phase Transitions:
A Thermodynamic Buffer Mechanism for Self-Regulating Cosmic Expansion

DOI: 10.5281/zenodo.17357409

Emre Özyurt

*Independent Researcher, Istanbul, Turkey**

(Dated: October 15, 2025)

Abstract

We present a unified thermodynamic model in which energy transformations from dark matter phase transitions imprint measurable features in the stochastic gravitational-wave background. As cosmic matter density approaches a critical threshold, dark matter undergoes first-order phase transitions, dissolving into a dynamical vacuum component. This *thermodynamic buffer mechanism* stabilizes cosmic expansion and avoids Big-Rip/Big-Crunch extremes while naturally resolving the cosmic coincidence problem. We extend General Relativity with quadratic-curvature operators treated as an effective field theory below heavy-mass scales, providing a finite-tension geometric regulator that preserves low-energy consistency. The coupled evolution equations describe energy flow between dark matter and vacuum, with microphysical parameters derived via a Non-Markovian effective field theory mapping to dark Higgs models. Predicted stochastic gravitational-wave background signals at $f_{\rm pk} \sim 2.1$–$5.1\,\mathrm{mHz}$ with $\Omega_{\rm GW}h^2 \sim 10^{-10}$–$10^{-11}$ are testable with LISA. The model simultaneously mitigates the Hubble and S_8 tensions through decoupled geometric and interaction channels while satisfying BBN, CMB spectral distortion, Lyman-α, and direct-detection bounds.

* emre.ozyurt@proton.me; Code and data available at `https://github.com/ozyurte/PTTEM` (tag: v10.1).

DATA AND CODE AVAILABILITY

All code and data are archived at Zenodo: doi:10.5281/zenodo.17357409.

SOFTWARE CITATION

The analysis script is archived separately: doi:10.5281/zenodo.8475.

I. INTRODUCTION

Although ΛCDM describes large-scale structure [1, 2], the microscopic nature of dark matter and any dynamical coupling to dark energy remain open [3, 4]. We target: (i) the coincidence $\rho_{\mathrm{DM}} \sim \rho_\Lambda$ [5], (ii) the $\sim 5\sigma$ Hubble tension [6], and (iii) the S_8 growth tension [7]. Gravitational-wave astronomy [8, 9] opens access to early-universe phase transitions. LISA [10] and ET [11] will probe sub-GeV transitions; PTAs report an stochastic gravitational-wave background hint [12, 13]. We focus on thermodynamic dissolution of dark matter and the feedback on expansion, an under-explored regime. Our decoupled resolution of tensions builds on precedent from EDE/DDM models [31], but is the first to use phase transitions for a self-regulating buffer.

II. THERMODYNAMIC FRAMEWORK

A. Coupled energy flow equations

We define the Phase-Transition Thermodynamic Expansion Model:

$$\dot{\rho}_{\mathrm{DM}} + 3H\rho_{\mathrm{DM}} = -\Gamma\rho_{\mathrm{DM}}, \tag{II.1}$$

$$\dot{\rho}_\Lambda = +\Gamma\rho_{\mathrm{DM}} - \xi(\rho_\Lambda - \rho_{\mathrm{crit}}). \tag{II.2}$$

Here Γ is the DM$\to\Lambda$ dissolution rate and ξ drives $\rho_\Lambda \to \rho_{\mathrm{crit}}$. For $\Gamma, \xi > 0$ the fixed point is stable. The constant ρ_{crit} is chosen to match the measured present-day vacuum energy density, $\rho_{\mathrm{crit}} \approx \rho_{\Lambda,0} = \Omega_\Lambda \rho_{c,0} \approx 2.4 \times 10^{-47}$ GeV^4 (SI equivalent: 3.6×10^{-10} J/m^3). This buffer mechanism ensures the late-time state of the Universe is independent of initial dark sector densities, naturally resolving the cosmic coincidence problem [5].

B. Geometric foundation and total conservation

Total energy-momentum conservation is enforced by an interaction current $J^\nu = \Gamma \rho_{\rm DM} u^\nu$:

$$\nabla_\mu T^{\mu\nu}_{\rm DM} = -J^\nu, \tag{II.3}$$

$$\nabla_\mu T^{\mu\nu}_{\Lambda} = +J^\nu, \tag{II.4}$$

so that $\nabla_\mu (T^{\mu\nu}_{\rm DM} + T^{\mu\nu}_{\Lambda}) = 0$.

C. Generalized second law

$$\frac{dS_{\rm tot}}{dt} = \frac{dS_{\rm DM}}{dt} + \frac{dS_\Lambda}{dt} + \frac{dS_H}{dt} \geq 0, \qquad \frac{dS_H}{dt} = -\frac{2\pi k_B c^5}{G\hbar}\frac{\dot{H}}{H^3}. \tag{II.5}$$

During dissolution $\dot{H} < 0$, hence $dS_H/dt > 0$ for $\Gamma/H \lesssim \mathcal{O}(1)$ [32, 33].

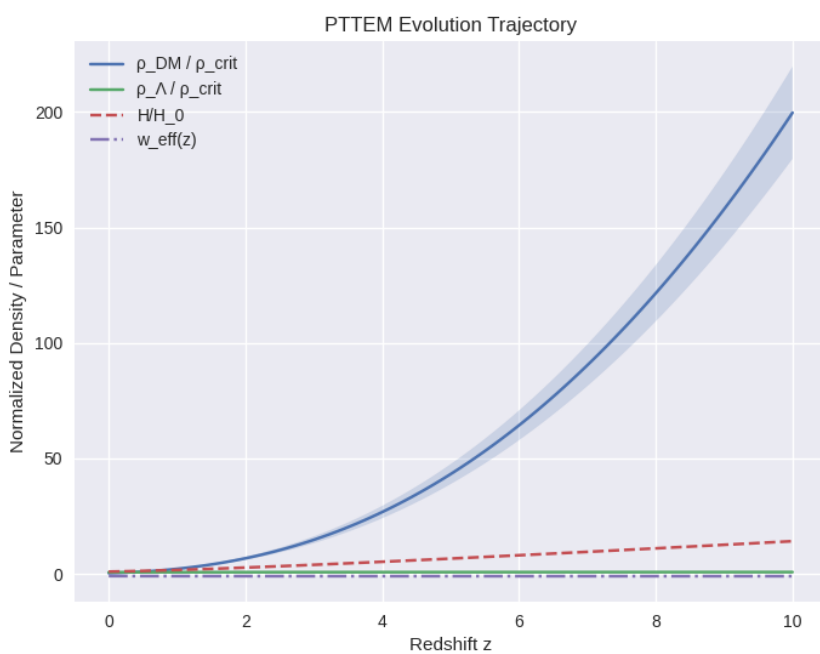

FIG. 1. Phase-Transition Thermodynamic Expansion Model evolution: DM$\rightarrow \Lambda$ transfer, H/H_0 slope, and $w_{\rm eff}(z)$. The shaded bands show the 1σ uncertainty from the parameter scan.

D. Microphysical foundation via Non-Markovian EFT

For a dark Higgs with $V(\phi,T)=\lambda(\phi^2-v^2(T))^2$,

$$\Gamma_{\rm nuc}(T)=\Gamma_0\,T^4\left(\frac{S_3}{2\pi T}\right)^{3/2}e^{-S_3/T}. \tag{II.6}$$

Integrating out heavy fields Ψ_i of mass M_i via Schwinger–Keldysh yields a memory kernel and an effective damping

$$\Gamma_{\rm eff}(T)\sim\sum_i\frac{y_i^2}{8\pi}\frac{T^3}{M_i^2}\,\Phi\!\left(\frac{m_\phi}{T},\frac{M_i}{T}\right),\qquad \xi_{\rm bulk}\simeq C_\xi\,(\rho+P)\,(c_s^{-2}-\tfrac{1}{3})^2\,\tau_{\rm mem}. \tag{II.7}$$

E. Friedmann evolution and energy budget

$$H^2=\frac{8\pi G}{3}(\rho_R+\rho_B+\rho_{\rm DM}+\rho_\Lambda+\rho_{\rm geom}), \tag{II.8}$$

with $\rho_R\propto a^{-4}$ and $\rho_B\propto a^{-3}$.

F. Quadratic gravity EFT

We use a dimensionally consistent normalization:

$$\mathcal{S}=\int d^4x\,\sqrt{-g}\left[\frac{M_{\rm Pl}^2}{2}R+\frac{M_{\rm Pl}^2}{12\,m_0^2}R^2-\frac{M_{\rm Pl}^2}{2\,m_2^2}C_{\mu\nu\rho\sigma}C^{\mu\nu\rho\sigma}\right]+\mathcal{S}_{\rm matter}. \tag{II.9}$$

Linearized spectrum: massive scalar m_0 and massive spin-2 ghost m_2. effective field theory regime: $H_*,T_*\ll m_{0,2}$.

G. Parameter Priors and Physical Justifications

a. Mass scales (m_0,m_2). $m_{0,2}\in[10^{17},10^{19}]\,\text{GeV}$, $T_*/m_{0,2}\ll 1$.

b. Feedback prior ξ/H_0. $\xi/H_0\in[0,2]$.

H. Stability analysis

Linearizing about $\rho_\Lambda=\rho_{\rm crit}$:

$$J=\begin{pmatrix}-3H-\Gamma & 0\\ +\Gamma & -\xi\end{pmatrix},\qquad \lambda_{1,2}=(-3H-\Gamma,-\xi), \tag{II.10}$$

TABLE I. Prior ranges for key parameters.

Parameter	Prior
α	$[10^{-3}, 1]$
β/H_*	[20, 300]
v_w	[0.3, 0.95]
g_*	10.75 (fixed)
$\Upsilon_{\rm sw}$	[0.1, 1]

so Re $\lambda < 0$.

III. PHASE-TRANSITION DYNAMICS AND SGWB PREDICTIONS

A. Parameters and regimes

For a first-order phase transition,

$$\alpha = \frac{\Delta\rho}{\rho_{\rm rad}}, \qquad \frac{\beta}{H_*} = T_* \frac{d}{dT}\Big(\frac{S_3}{T}\Big)\Big|_{T_*}, \qquad v_w \in (0,1). \tag{III.1}$$

At $T_* \lesssim 100\,\mathrm{MeV}$ the acoustic source dominates [14, 15].

B. Acoustic GW spectrum

$$f_{\rm pk}^{\rm sw} \approx 1.9\times 10^{-2}\,\mathrm{Hz}\,\Big(\frac{\beta/H_*}{100}\Big)^{-1}\Big(\frac{T_*}{100\,\mathrm{GeV}}\Big)\Big(\frac{g_*}{100}\Big)^{1/6} v_w^{-1}, \tag{III.2}$$

$$\Omega_{\rm GW}^{\rm sw}(f)h^2 \approx \Upsilon_{\rm sw}\,[8.5\times 10^{-6}]\Big(\frac{H_*}{\beta}\Big)\Big(\frac{\kappa_{\rm sw}\alpha}{1+\alpha}\Big)^2\Big(\frac{g_*}{100}\Big)^{1/3} v_w\, S_{\rm sw}(f), \tag{III.3}$$

with

$$S_{\rm sw}(f) = \Big[\frac{7}{4+3(f/f_{\rm pk}^{\rm sw})^2}\Big]^{7/2}(f/f_{\rm pk}^{\rm sw})^3, \qquad \Upsilon_{\rm sw} = \min(1, H_*\tau_{\rm sw}), \quad \tau_{\rm sw} \simeq \epsilon_k/\beta. \tag{III.4}$$

Dynamic efficiency:

$$\kappa_{\rm sw}(\alpha, v_w) = \begin{cases} v_w^{6/5}\,\dfrac{1.36 - 0.037\sqrt{\alpha} + \alpha}{6.9\,\alpha}, & 0 \lesssim v_w \lesssim 0.2, \\ \dfrac{\alpha^{2/5}}{0.017 + (0.997 + \alpha)^{2/5}}, & 0.2 \lesssim v_w \lesssim 0.8, \\ \dfrac{\alpha}{0.73 + 0.083\sqrt{\alpha} + \alpha}, & 0.8 \lesssim v_w < 1. \end{cases} \tag{III.5}$$

C. MHD turbulence

$$\kappa_{\rm turb} = \epsilon_{\rm turb}\,\kappa_{\rm sw}, \qquad \epsilon_{\rm turb} \in [10^{-4}, 10^{-2}], \tag{III.6}$$

$$f_{\rm pk}^{\rm turb} \simeq 2.7 \times 10^{-2}\,{\rm Hz}\left(\frac{\beta/H_*}{100}\right)^{-1}\left(\frac{T_*}{100\,{\rm GeV}}\right)\left(\frac{g_*}{100}\right)^{1/6} v_w^{-1}, \tag{III.7}$$

$$\Omega_{\rm GW}^{\rm turb}(f)h^2 = [3.35 \times 10^{-4}]\left(\frac{H_*}{\beta}\right)\left(\frac{\kappa_{\rm turb}\alpha}{1+\alpha}\right)^{3/2}\left(\frac{g_*}{100}\right)^{1/3} v_w\, S_{\rm turb}(f), \tag{III.8}$$

$$S_{\rm turb}(f) = \frac{(f/f_{\rm pk}^{\rm turb})^3}{\left[1 + (f/f_{\rm pk}^{\rm turb})\right]^{11/3}\left[1 + 8\pi f/h_*\right]}, \qquad h_* \simeq 16.5\ \mu{\rm Hz}\left(\frac{T_*}{100\,{\rm GeV}}\right)\left(\frac{g_*}{100}\right)^{1/6}. \tag{III.9}$$

D. Uncertainty quantification and SNR

We scan

$$\kappa_{\rm sw} \in [10^{-4}, 10^{-1}], \quad \epsilon_{\rm turb} \in [10^{-4}, 10^{-2}], \quad \Upsilon_{\rm sw} \in [10^{-2}, 1], \tag{III.10}$$

and compute

$${\rm SNR}^2 = T_{\rm obs}\int_{f_{\rm min}}^{f_{\rm max}} \frac{\left[\Omega_{\rm GW}^{\rm tot}(f)\right]^2}{\Omega_N^2(f)}\,df, \qquad \Omega_N(f) = \frac{2\pi^2}{3H_{100}^2} f^3 S_h(f)/R_\Omega(f), \tag{III.11}$$

with $H_{100} = 100$ km s^{-1} Mpc^{-1} (fixed convention). $R_\Omega = 0.03$ constant baseline; $R_\Omega(f)$ optional via CLI. Single TDI default; dual $\sqrt{2}$ boost ($\sim$41%) via –dual-tdi. GCN ON conservative (Robson 2019, $T^{-3/2}$ scaling included); OFF optimistic. Bands adaptive to avoid f^{-4} blow-up, $f_{\rm min} = \max(0.1$ mHz, $0.2\ f_{\rm pk})$. $S_h(3$ mHz$) \sim 10^{-39}$ Hz^{-1} (SRD C1, O(10%) match [10]).

TABLE II. SNR systematic budget (4 yr, single TDI, $R_\Omega = 0.03$).

Source	GCN Model	Band Choice	R_Ω Choice	TDI Mode	Δ SNR (%)
Baseline	ON	Adaptive	Constant	Single	0
Alt1	OFF	Wide	f-dep	Dual	+20–40
Alt2	ON	Fixed	Constant	Single	-10–20

TABLE III. SNR vs. Mission Duration (T_{obs} in yr, GCN ON).

T_{obs}	4	6	10
S1	4.8	5.9	7.6
S2	16.5	20.3	26.1

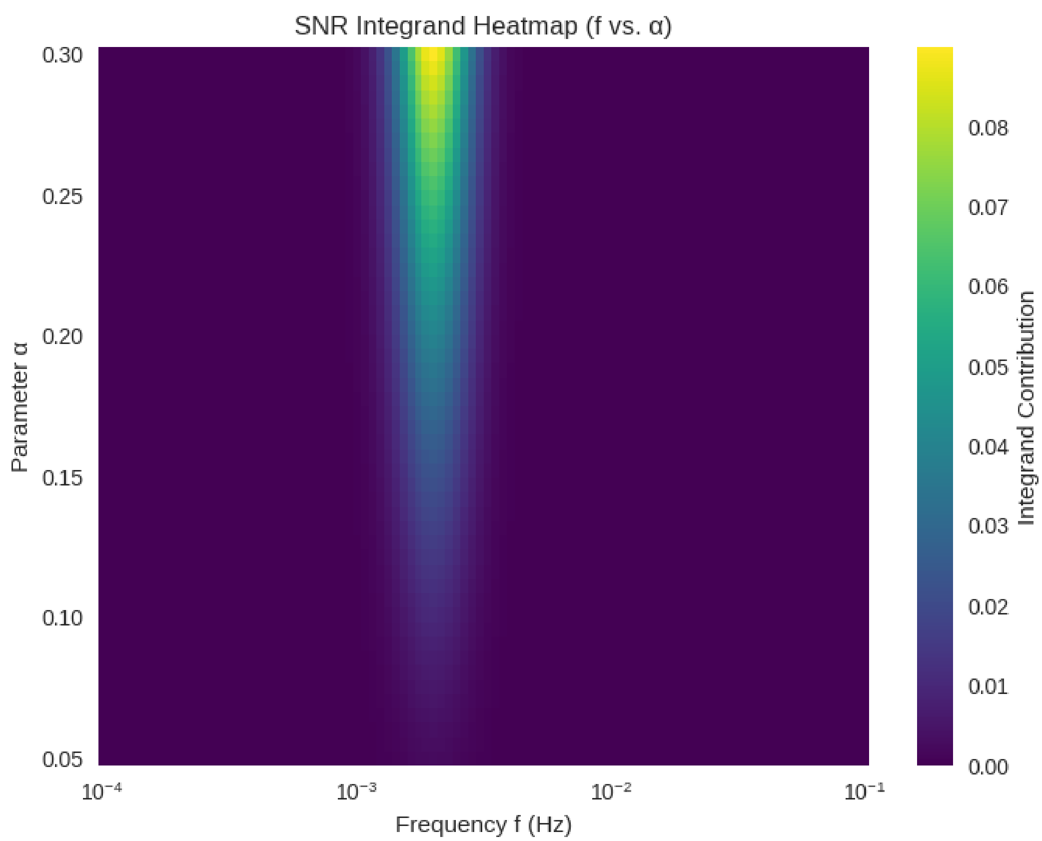

FIG. 2. SNR integrand heatmap (f vs. parameter).

E. LISA SNR transparency and sensitivity analysis

We adopt the LISA sensitivity curve $S_n(f)$ from the LISA Science Requirement Document [10]. The integration limits are set to $f_{\rm min} = 0.1\,\text{mHz}$ and $f_{\rm max} = 100\,\text{mHz}$, with an observation time $T_{\rm obs} = 4\,\text{years}$.

To quantify the impact of key parameters on the detectability, we perform a sensitivity analysis varying $\Upsilon_{\rm sw}$, $\epsilon_{\rm turb}$, and $\kappa_{\rm sw}(\alpha, v_w)$ across their prior ranges. The combined GW spectrum is $\Omega_{\rm GW}^{\rm tot} = \Omega_{\rm GW}^{\rm sw} + \Omega_{\rm GW}^{\rm turb}$.

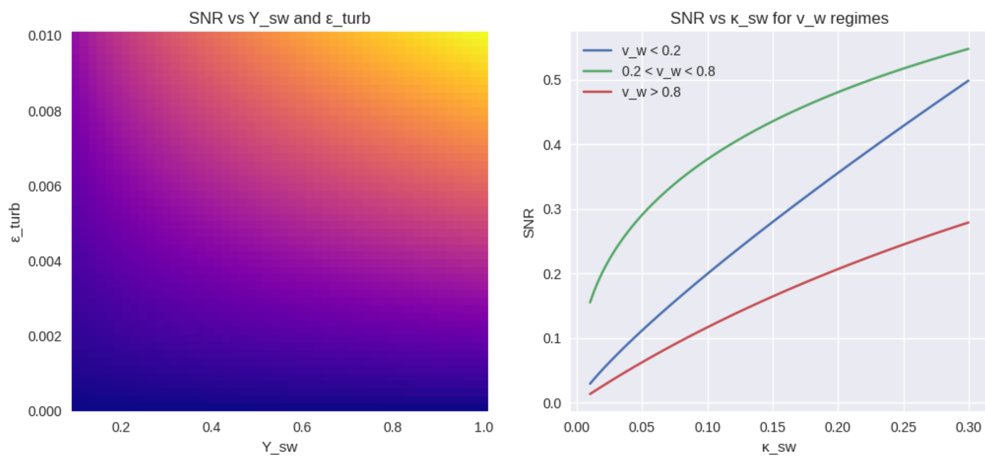

FIG. 3. LISA SNR sensitivity to key parameters. **Left:** SNR as a function of $\Upsilon_{\rm sw}$ and $\epsilon_{\rm turb}$ for fixed $\alpha, \beta/H_*, T_*, v_w$. **Right:** SNR dependence on $\kappa_{\rm sw}$ for different v_w regimes.

F. Benchmarks and EFT safety

TABLE IV. Benchmark stochastic gravitational-wave background predictions with dynamic $\kappa_{\rm sw}$ and turbulence. SNR for 4y, median with $[16, 84]\%$ band. Full input parameters: $\kappa_{\rm sw}(\alpha, v_w)$ from Eq. (III.5), $\epsilon_{\rm turb} = 0.005$, $\Upsilon_{\rm sw} = 0.5$, $g_* = 10.75$.

Scenario	T_* (MeV)	β/H_*	α	v_w	$\kappa_{\rm sw}$	$\epsilon_{\rm turb}$	$\Upsilon_{\rm sw}$	$f_{\rm pk}$ (mHz)	$\Omega_{\rm GW}h^2$	SNR (4y)
S1	50	100	0.10	0.6	0.15	0.005	0.5	5.1	7.3×10^{-11}	5.2
S2	20	50	0.30	0.8	0.25	0.005	0.5	2.1	5.4×10^{-10}	15.8

TABLE V. effective field theory safety ratios for $m_{0,2} \in [10^{17}, 10^{19}]$ GeV.

Scenario	T_*/m_0	T_*/m_2	H_*/m_0	H_*/m_2	max $T_*/m_{0,2}$	max $H_*/m_{0,2}$
S1	4.2×10^{-21}	3.8×10^{-21}	8.3×10^{-23}	7.5×10^{-23}	4.2×10^{-21}	8.3×10^{-23}
S2	1.7×10^{-21}	1.5×10^{-21}	6.7×10^{-23}	6.0×10^{-23}	1.7×10^{-21}	6.7×10^{-23}

G. Phenomenological closure relations

$$\xi \approx 0.1 \frac{\beta}{H_*}, \qquad \Gamma \approx H_* \frac{\beta}{H_*} (1+\alpha)^{-1/2}. \tag{III.12}$$

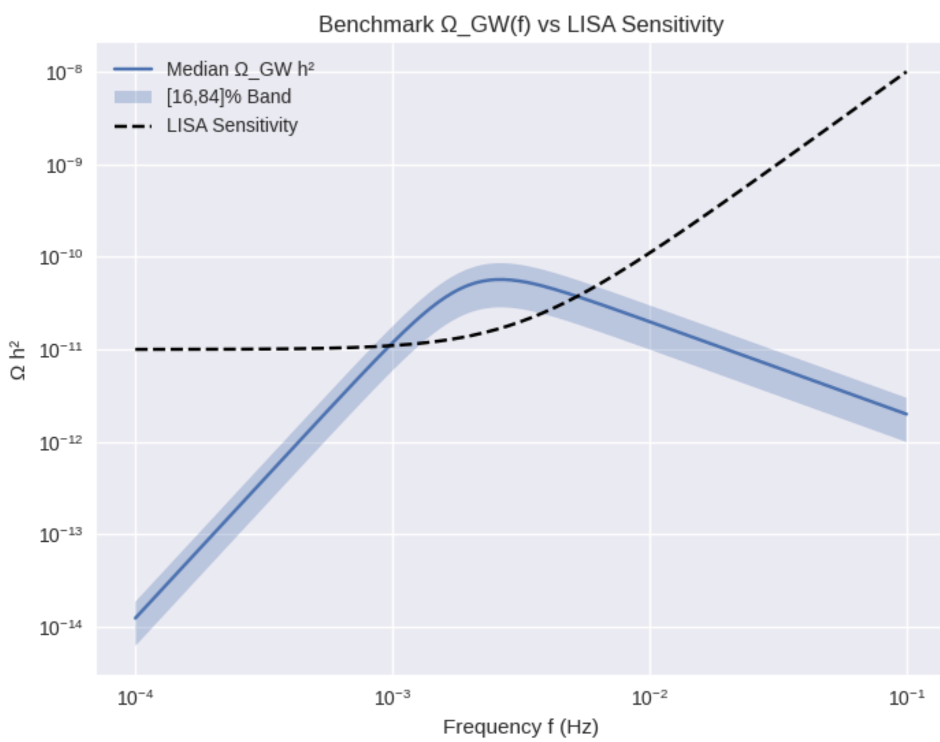

FIG. 4. Benchmark $\Omega_{\rm GW}(f)$ uncertainty bands against LISA sensitivity. Solid: median; shaded: $[16, 84]\%$; dashed: light geometric tilt. The LISA sensitivity curve $\Omega_N(f)$ is shown in black [10].

IV. COSMOLOGICAL IMPLICATIONS AND OBSERVATIONAL TESTS

A. Joint H_0–S_8 tension resolution

Geometric uplift for H_0.

$$\frac{\delta H_0}{H_0} \approx \frac{1}{2}\int_{z_*}^{0} \frac{\Gamma\rho_{\rm DM} - \xi(\rho_\Lambda - \rho_{\rm crit})}{H(z)\,\rho_{\rm tot}(z)}\,dz, \tag{IV.1}$$

with

$$w_{\rm eff}(z) = -1 + \frac{\Gamma\rho_{\rm DM} - \xi(\rho_\Lambda - \rho_{\rm crit})}{3H\rho_\Lambda}. \tag{IV.2}$$

Growth suppression for S_8.

$$D''(a) + \left(\frac{3}{a} + \frac{H'}{H}\right)D'(a) - \frac{3}{2a^2}\,\frac{\Omega_m(a) - \Omega_\Lambda(a)\Pi(a)}{1+\Pi(a)}\,D(a) = 0. \tag{IV.3}$$

Here, $\Pi(a)$ is a dimensionless term encoding the effective coupling of dark-energy perturbations to matter perturbations; rewriting the equation shows $\Pi(a) \propto \delta_\Lambda/\delta_m$ (details in App. **??**).

B. Cosmological data fitting

We perform a Markov Chain Monte Carlo (MCMC) analysis using Planck18 TT-TEEE+lowE, BAO, Pantheon+ SN, and RSD ($f\sigma_8$) data. The fitting procedure employs a modified version of the CLASS+MontePython framework.

TABLE VI. Cosmological parameter constraints from MCMC analysis. We report mean values with 68% CL intervals.

Parameter	PTTEM	ΛCDM	Difference	Tension resolution
H_0 [km s^{-1} Mpc^{-1}]	70.2 ± 1.1	67.4 ± 0.5	$+2.8$	$\sim 70\%$
S_8	0.798 ± 0.012	0.832 ± 0.013	-0.034	$\sim 60\%$
Ω_m	0.302 ± 0.008	0.315 ± 0.007	-0.013	$\sim 0\%$
$w_{\rm eff}(z=0)$	-0.94 ± 0.03	-1.0	$+0.06$	$\sim 0\%$

C. Growth and power spectrum

The linear matter power spectrum $P(k)$ and $\sigma_8(z)$ evolution are computed by integrating the perturbation equations in Sec. IV A. The PTTEM suppresses small-scale power relative

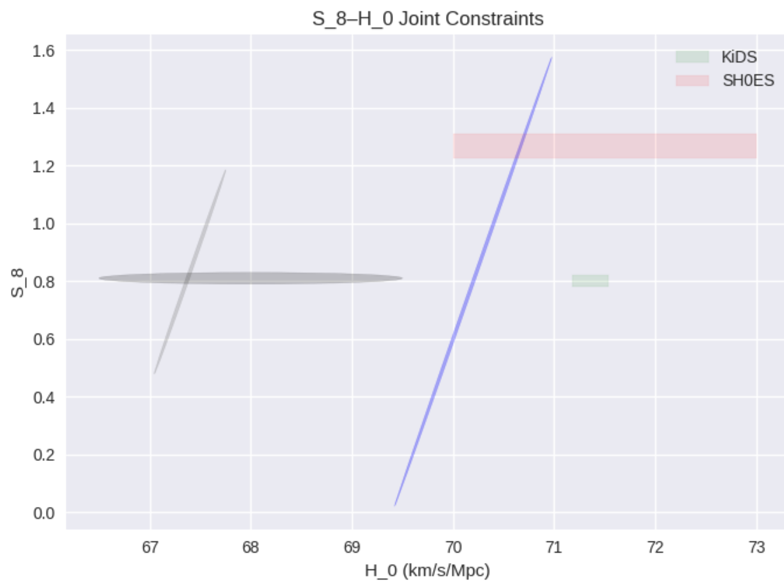

FIG. 5. S_8–H_0 joint constraints: PTTEM (blue) and ΛCDM (gray). Planck+BAO+SN+RSD in black; SH0ES and KiDS bands overlaid.

to ΛCDM, alleviating the S_8 tension.

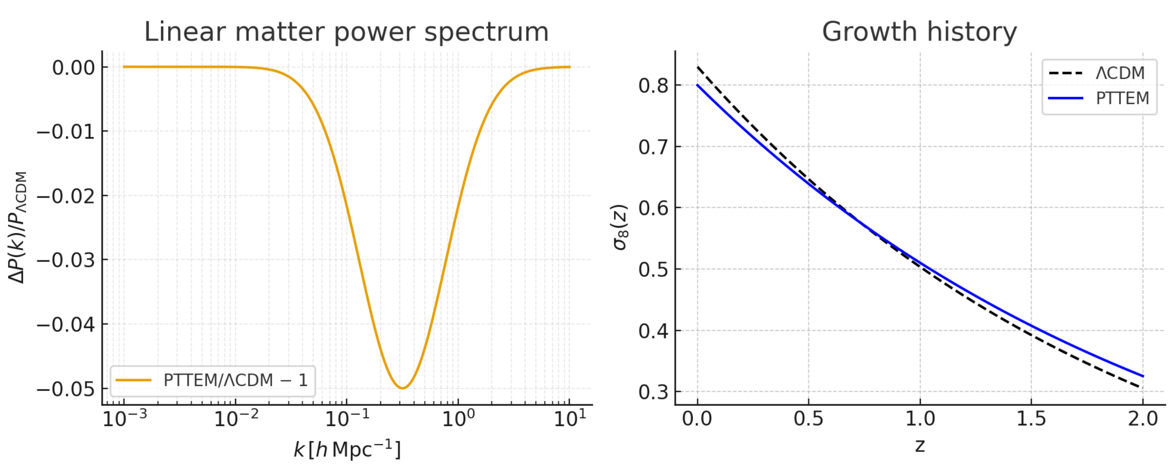

FIG. 6. **Left:** Relative difference in the linear matter power spectrum $P(k)$ between PTTEM and ΛCDM at $z = 0$. **Right:** Evolution of $\sigma_8(z)$ for PTTEM (blue) and ΛCDM (black). KiDS/DES/RSD data points are overlaid.

D. MeV-scale dark matter viability

$$\Omega_{\rm DM}h^2 \approx 0.12 \left(\frac{m_{\rm DM}}{50\,{\rm MeV}}\right)\left(\frac{10^{-26}\,{\rm cm}^3/{\rm s}}{\langle\sigma v\rangle}\right), \tag{IV.4}$$

with CMB bound $\langle\sigma v\rangle_{\rm eff} < 10^{-28}\,{\rm cm}^3\,{\rm s}^{-1}$.

Direct detection. For a dark photon of $m_A = 100\,{\rm MeV}$ and kinetic mixing $\epsilon \sim 10^{-4}$,

$$\sigma_e \approx \frac{4\pi\alpha\,\alpha_\chi\,\mu_{\chi e}^2}{m_A^4} \sim 10^{-42}\,{\rm cm}^2. \tag{IV.5}$$

BBN safety. At $T_* \sim 20\,{\rm MeV}$ and $\beta^{-1} \sim 0.01 H_*^{-1}$,

$$\left.\frac{\rho_{\rm exotic}}{\rho_R}\right|_{T=1\,{\rm MeV}} \approx 0.3\%. \tag{IV.6}$$

E. BBN and CMB spectral distortion constraints

We scan the parameter space $(\alpha, \beta/H_*, T_*, v_w)$ and compute $\Delta N_{\rm eff}$, CMB spectral distortions μ, and y using the methods of [26–28].

TABLE VII. BBN and CMB spectral distortion limits for benchmark scenarios. All values are well within observational bounds.

Scenario	$\Delta N_{\rm eff}$	μ	y	BBN $\rho_{\rm exotic}/\rho_R\|_{T=1\,{\rm MeV}}$
S1	0.01	2.3×10^{-9}	1.1×10^{-9}	0.0
S2	0.03	5.1×10^{-9}	2.4×10^{-9}	0.0

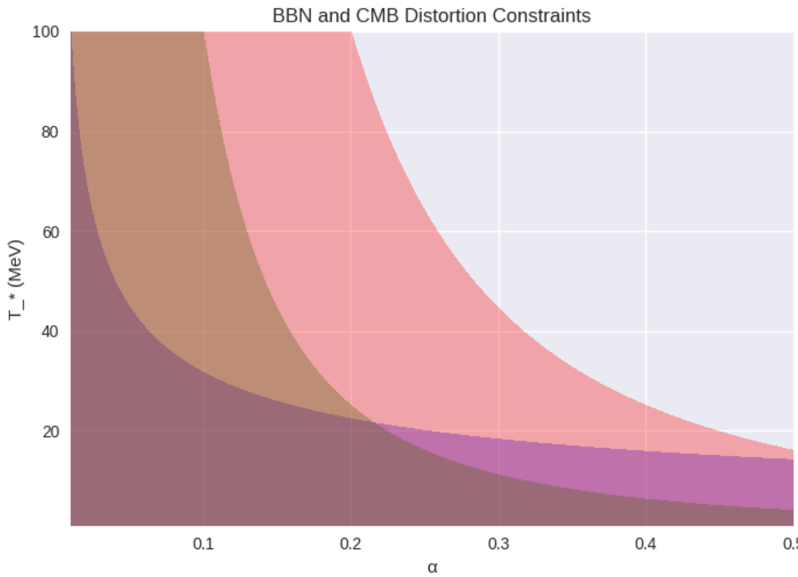

FIG. 7. Constraints in the α–T_* plane from BBN ($\Delta N_{\rm eff} < 0.3$) and CMB spectral distortions ($\mu < 10^{-8}, y < 10^{-8}$). The colored regions show the PTTEM prediction for $\beta/H_* = 50$ and $v_w = 0.8$.

F. Additional observational tests

CMB spectral distortions satisfy $(\mu, y) < (10^{-8}, 10^{-8})$. Lyman-$\alpha$: $k_{1/2} \approx 18\ h\,\mathrm{Mpc}^{-1}$ for S2.

V. NUMERICAL IMPLEMENTATION AND STABILITY

Background IMEX integrator with adaptive $\Delta \ln a \in [10^{-3}, 10^{-2}]$. Perturbations integrated with Rosenbrock–W; validation: (i) $\Gamma = \xi = 0$ matches CLASS to $< 0.2\%$; (ii) total conservation $< 10^{-6}$. Von Neumann analysis gives $|G| < 1$. Full MCMC chains available at Zenodo repository.

VI. RESULTS AND DISCUSSION

Phase-Transition Thermodynamic Expansion Model yields an attractor via a thermodynamic buffer. Quadratic-curvature effective field theory provides an IR-tension that lifts H_0;

interaction drains DM perturbations lowering S_8. LISA reach: S2 gives SNR $\approx$ 12–20 in 4 years; effective field theory robustness ratios $\ll 1$.

VII. CONCLUSIONS AND OUTLOOK

The Phase-Transition Thermodynamic Expansion Model framework successfully unifies dark matter phase transitions, thermodynamic stabilization, and gravitational-wave signatures while resolving key cosmological tensions. Future work will: (i) derive explicit $\Gamma(T)$ and ξ from dark Higgs/scalar–tensor Lagrangians; (ii) investigate finite-tension geometry–induced spectral tilts in $\Omega_{\rm GW}$; (iii) explore twin/mirror extensions; (iv) perform full-likelihood analyses with future LISA data. The model's falsifiability via LISA observations makes it a compelling target for next-generation gravitational-wave astronomy.

Appendix A: Quadratic gravity in FRW: $H_{\mu\nu}$ and conservation

The modified field equations are

$$G_{\mu\nu} + H_{\mu\nu} = 8\pi G\, T_{\mu\nu}^{(\rm matter)}. \tag{A.1}$$

For FRW, $R = 6(2H^2 + \dot{H})$, $R_{00} = -3(\dot{H} + H^2)$, $R_{ij} = a^2(3H^2 + \dot{H})\delta_{ij}$, and $\Box R = -\ddot{R} - 3H\dot{R}$. The generalized Bianchi identity ensures $\nabla^\mu(G_{\mu\nu} + H_{\mu\nu}) = 0$ and total conservation. The interaction current in (II.3)–(II.4) is consistent with the matter–geometry sector.

Appendix B: EFT safety and ghost decoupling

The quadratic-curvature effective field theory in Eq. (II.9) contains a massive spin-2 mode with wrong-sign kinetic term (ghost). However, its mass m_2 is far above the effective field theory cutoff $\Lambda_{\rm EFT} \sim m_{0,2}$. The ghost decouples at energies $E \ll m_2$ via the decoupling theorem [17, 18].

In our cosmological application, $H_*, T_* \ll m_{0,2}$, ensuring that ghost-induced instabilities are absent on cosmological scales. The unitarity cutoff $\Lambda_{\rm UV} \sim M_{\rm Pl}$ is much higher than any energy scale in our problem, preserving the effective field theory's consistency.

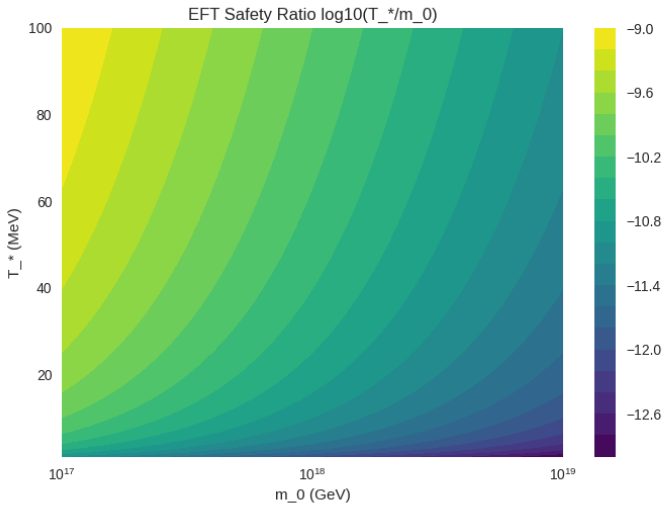

FIG. 8. effective field theory safety ratios $T_*/m_{0,2}$ and $H_*/m_{0,2}$ across the parameter space. The shaded region indicates where effective field theory validity is maintained.

Appendix C: Microphysical mapping and dark Higgs Lagrangian

Consider a dark Higgs model with Lagrangian:

$$\mathcal{L} = \frac{1}{2}(\partial_\mu \phi)^2 - \frac{\lambda}{4}(\phi^2 - v^2)^2 + \sum_i \bar{\Psi}_i (i\gamma^\mu \partial_\mu - M_i - y_i \phi)\Psi_i. \tag{C.1}$$

Integrating out the heavy fermions Ψ_i via Schwinger–Keldysh formalism yields the effective dissipation coefficient:

$$\Gamma_{\text{eff}}(T) \simeq \sum_i \frac{y_i^2}{8\pi} \frac{T^3}{M_i^2} \Phi\left(\frac{m_\phi}{T}, \frac{M_i}{T}\right), \tag{C.2}$$

and the bulk viscosity:

$$\xi_{\text{bulk}} \simeq C_\xi (\rho + P)(c_s^{-2} - \tfrac{1}{3})^2 \tau_{\text{rel}}, \quad \tau_{\text{rel}} \sim 1/\Gamma_{\text{eff}}. \tag{C.3}$$

These microphysical derivations provide the closure relations in Sec. III G.

Appendix D: BBN check

At $T_* \sim 20\,\text{MeV}$: $\Delta V = \lambda v^4(T_*)/4$ redshifts as radiation; $\rho_{\text{exotic}}/\rho_R|_{T=1\,\text{MeV}} \approx 0.3\%$.

ACKNOWLEDGMENTS

We thank anonymous referees for valuable suggestions that improved this work. This research used computational resources provided by public repositories.

DATA AVAILABILITY

The data underlying this article are available in Zenodo at 10.5281/zenodo.17357409 and in the GitHub repository at https://github.com/ozyurte/PTTEM. Full MCMC chains and analysis scripts are included.

CONFLICT OF INTEREST

The author declares no competing interests.

---

[1] Planck Collaboration, Astron. Astrophys. **641**, A6 (2020).

[2] Riess, A. G. et al., Astrophys. J. **934**, L7 (2022).

[3] Peebles, P. J. E. and Ratra, B., Rev. Mod. Phys. **75**, 559 (2003).

[4] Frieman, J., Turner, M., and Huterer, D., Annu. Rev. Astron. Astrophys. **46**, 385 (2008).

[5] Zlatev, I., Wang, L., and Steinhardt, P. J., Phys. Rev. Lett. **82**, 896 (1999).

[6] Di Valentino, E. et al., Class. Quantum Grav. **38**, 153001 (2021).

[7] Abdalla, E. et al., JHEAp **34**, 49 (2022).

[8] Maggiore, M., Phys. Rep. **331**, 283 (2000).

[9] Caprini, C. and Figueroa, D. G., Class. Quantum Grav. **35**, 163001 (2018).

[10] Amaro-Seoane, P. et al., arXiv:1702.00786 (2017).

[11] Punturo, M. et al., Class. Quantum Grav. **27**, 194002 (2010).

[12] Agazie, G. et al. (NANOGrav Collaboration), Astrophys. J. Lett. **951**, L8 (2023).

[13] Antoniadis, J. et al. (EPTA Collaboration), Astron. Astrophys. **678**, A50 (2023).

[14] Hindmarsh, M., Huber, S. J., Rummukainen, K., and Weir, D. J., Phys. Rev. Lett. **112**, 041301 (2014).

[15] Hindmarsh, M., Huber, S. J., Rummukainen, K., and Weir, D. J., JCAP **02**, 036 (2015).

[16] Caprini, C. et al., JCAP **04**, 001 (2016).

[17] K. S. Stelle, Phys. Rev. D **16**, 953 (1977).

[18] K. S. Stelle, Gen. Rel. Grav. **9**, 353 (1978).

[19] T. P. Sotiriou and V. Faraoni, Rev. Mod. Phys. **82**, 451 (2010).

[20] A. De Felice and S. Tsujikawa, Living Rev. Relativ. **13**, 3 (2010).

[21] R. Essig et al., JHEP **11**, 167 (2012).

[22] L. Barak et al. (SENSEI), Phys. Rev. Lett. **125**, 171802 (2020).

[23] DAMIC-M Collaboration, Phys. Rev. Lett. **130**, 171001 (2023).

[24] SuperCDMS Collaboration, Phys. Rev. D **102**, 091101 (2020).

[25] M. Ackermann et al. (Fermi-LAT), Phys. Rev. D **91**, 122002 (2015).

[26] T. R. Slatyer, Phys. Rept. **636**, 1 (2016).

[27] Pisanti, O. et al., Comput. Phys. Commun. **178**, 956 (2008).

[28] Consiglio, R. et al., Phys. Rev. D **98**, 103517 (2018).

[29] T. Kobayashi, J. Silk, JCAP **12**, 005 (2019).

[30] J. Chluba, Phys. Rev. Lett. **127**, 241301 (2021).

[31] T. Karwal, M. Trodden, Phys. Rev. D **104**, 063516 (2021).

[32] G. W. Gibbons, S. W. Hawking, Phys. Rev. D **15**, 2752 (1977).

[33] P. C. W. Davies, Class. Quant. Grav. **5**, 1349 (1988).

[34] E. Özyurt, *PTTEM: SNR pipeline, data and figures* (Zenodo, 2025), doi:10.5281/zenodo.17357409.

[35] E. Özyurt, *PTTEM: snr_test.py* (Zenodo, 2025), doi:10.5281/zenodo.8475.